AGU PUBLICATIONS

JGR

Journal of Geophysical Research: Atmospheres

RESEARCH ARTICLE
10.1002/2015JD023403

**Key Points:**
- Water vapor isotope ratios identify convective precipitation efficiency
- Distinct circulation patterns result in precipitation efficiency differences
- High precipitation efficiency is associated with aerosol scavenging

**Supporting Information:**
- Text S1, Table S1, and Figure S1

**Correspondence to:**
A. Bailey,
adriana.bailey@colorado.edu

**Citation:**
Bailey, A., J. Nusbaumer, and D. Noone (2015), Precipitation efficiency derived from isotope ratios in water vapor distinguishes dynamical and microphysical influences on subtropical atmospheric constituents, *J. Geophys. Res. Atmos.*, *120*, doi:10.1002/2015JD023403.

Received 23 MAR 2015
Accepted 8 AUG 2015
Accepted article online 13 AUG 2015



# Precipitation efficiency derived from isotope ratios in water vapor distinguishes dynamical and microphysical influences on subtropical atmospheric constituents

**A. Bailey[1,2], J. Nusbaumer[1], and D. Noone[1,3]**

[1]Cooperative Institute for Research in Environmental Sciences and Department of Atmospheric and Oceanic Sciences, University of Colorado, Boulder, Colorado, USA, [2]Now at Joint Institute for the Study of the Atmosphere and Ocean, University of Washington, Seattle, Washington, USA, [3]College of Earth, Ocean, and Atmospheric Sciences, Oregon State University, Corvallis, Oregon, USA

**Abstract** With water vapor and clouds expected to effect significant feedbacks on climate, moisture transport through convective processes has important implications for future temperature change. The precipitation efficiency—the ratio of the rates at which precipitation and condensation form ($e = P/C$)—is useful for characterizing how much boundary layer moisture recycles through precipitation versus mixes into the free troposphere through cloud detrainment. Yet it is a difficult metric to constrain with traditional observational techniques. This analysis characterizes the precipitation efficiency of convection near the Big Island of Hawaii, USA, using a novel tracer: isotope ratios in water vapor. The synoptic circulation patterns associated with high and low precipitation efficiency are identified, and the importance of large-scale dynamics and local convective processes in regulating vertical distributions of atmospheric constituents important for climate is evaluated. The results suggest that high $e$ days are correlated with plume-like transport originating from the relatively clean tropics, while low $e$ days are associated with westerly transport, generated by a branching of the jet stream. Differences in transport pathway clearly modify background concentrations of water vapor and other trace gases measured at Mauna Loa Observatory; however, local convective processes appear to regulate aerosols there. Indeed, differences between observed and simulated diurnal cycles of particle number concentration indicate that precipitation scavenges aerosols and possibly facilitates new particle formation when $e$ is high. As measurements of isotope ratios in water vapor expand across the subtropics, the techniques presented here can further our understanding of how synoptic weather, precipitation processes, and climate feedbacks interrelate.

## 1. Introduction

Shallow convection plays a critical role in climate by regulating the exchange of moisture between the boundary layer and free troposphere. While convective activity results in a net upward transport of moisture, precipitation works to dry the atmosphere by removing condensate and returning liquid water to the surface [*Sherwood et al*., 2010]. The efficiency with which a convective cloud system produces precipitation (i.e., the precipitation efficiency or $e$) thus determines the proportion of water detrained above the boundary layer through cloud evaporation. Not all studies agree, however, as to how the precipitation efficiency affects low-level cloudiness. *Sherwood et al.* [2014], for example, hypothesized that as convective mixing in the lower troposphere increases, moistening of the free troposphere occurs at the expense of the boundary layer and the bulk precipitation efficiency is reduced. Drying of the boundary layer subsequently reduces low-level cloud and enhances climate warming. *Zhao* [2014], in contrast, claimed that climate models with lower precipitation efficiency maintain higher liquid water paths and thus exhibit greater low-cloud cover, which reduces warming through albedo effects. To help resolve these divergent hypotheses, observational assessments of precipitation efficiency and cloud fields are needed.

In addition to modifying moisture exchange in the vertical, cloud and precipitation processes influence climate by regulating vertical distributions of aerosols. Precipitation is the principal mechanism by which aerosols are cleansed from the atmosphere [*Ramanathan et al*., 2001], and recent work suggests that rain removal is more important than proximity to an emission source in determining particle number concentrations near marine low cloud [*Wood et al*., 2012]. Some particle scavenging may, however, be offset by new particle formation, since the removal of preexisting particles reduces the vapor condensation sink for

aerosol-forming gases like $H_2SO_4$ [cf. *Nilsson et al.*, 2001]. Consequently, recently formed particles are often observed in the vicinity of precipitating convective systems [*Clarke*, 1993]. In contrast, when precipitation is absent, cloud processing can enhance particle number concentrations above the boundary layer [*Ridley et al.*, 1997] and shift particles toward larger diameters [*Hoppel et al.*, 1986]. Such changes have repercussions for Earth's radiative energy balance, since both concentration and size influence aerosol optical properties [*Yu et al.*, 2006]. Moreover, changes in particle concentration can influence climate indirectly by modifying cloud albedo [*Twomey*, 1977] and cloud precipitation efficiency—with possible consequences for cloud amount [*Albrecht*, 1989]. This coupling between aerosols, cloud microphysical structure, and precipitation complicates efforts to distinguish cause and effect when studying cloud feedbacks on climate [*Stevens and Feingold*, 2009].

A key challenge in evaluating interactions between aerosols, clouds, and precipitation is that using observations to quantify precipitation efficiency is no small task. To estimate precipitation efficiency using satellite retrievals of rainfall and cloud liquid water content, for instance, *Lau and Wu* [2003] required a weather and climate model parameterization, which assumes that the autoconversion of cloud drops to raindrops depends on a critical value of cloud water content. Other observational estimates of precipitation efficiency require knowledge of large-scale hydrological fields, such as water vapor convergence and surface evaporation [*Sui et al.*, 2005, 2007], which cannot be measured directly. To evaluate the relationships among convective mixing, precipitation, aerosols, and cloudiness, a simple method for estimating precipitation efficiency is desirable.

Isotope ratios in water vapor provide a unique way to characterize the precipitation efficiency of convection [*Bailey et al.*, 2013] since heavy isotopes—with their lower saturation vapor pressures—preferentially and predictably condense and rain out [*Dansgaard*, 1964]. The more efficiently precipitation forms (i.e., the closer the rates of precipitation and condensation), the larger the depletion of heavy isotopes from the cloud system [*Dansgaard*, 1964; *Jouzel and Merlivat*, 1984; *Noone*, 2012]. This isotopic record is conserved and advected with the dominant atmospheric motion in the absence of air mass mixing [*Gedzelman*, 1988]. Importantly, pairing measurements of humidity with isotopic observations creates the diagnostic power necessary to distinguish isotopic changes due to mixing from changes due to clouds and precipitation [*Noone*, 2012].

This study uses spectroscopic measurements of water vapor volume mixing ratios and isotope ratios in water vapor to identify synoptic controls on the precipitation efficiency of boundary layer convection near Hawaii and to determine the influence of dynamical and microphysical (precipitation) processes on vertical distributions of atmospheric constituents important for climate. First, the ability of Eulerian measurements to characterize precipitation efficiency is established using a 3 year record from the Mauna Loa Observatory (Hawaii, USA). Then, the association between large-scale circulation and convection with high or low precipitation efficiency is evaluated. By linking local precipitation characteristics with large-scale fields well resolved by climate models, the analysis reveals how the bulk precipitation efficiency of the subtropics may change with climate. Finally, the strength of vertical mixing associated with convection of different precipitation efficiencies is modeled in order to distinguish dynamical and microphysical controls on vertical distributions of moisture, trace gases, and particle pollutants. The results suggest that while variations in synoptic circulation influence the trace gas concentrations observed, vertical mixing and microphysical processes—which also vary by precipitation efficiency—are more important in regulating particle scavenging and growth.

## 2. Methods

### 2.1. Location

Mauna Loa Observatory (MLO; 19.5362°N, 155.5763°W), located at 3400 m elevation on the Big Island of Hawaii, has served as a baseline observatory since the 1950s, measuring key climate-altering constituents including numerous greenhouse gases. With its remote Pacific setting and high-altitude location, MLO is often exposed to the free troposphere at night. Yet, during the day, convection transports boundary layer air to heights exceeding the Observatory's through a combination of buoyant forcing [e.g., *Kleissl et al.*, 2007] and cloud detrainment, thereby modifying the concentrations of trace gases and aerosols measured there. Air masses defining the top of the boundary layer arrive at MLO first, followed by air masses from successively lower heights, creating diurnal variations in the Eulerian measurements that essentially reflect the vertical distributions of the atmospheric column. Measurements of isotope ratios at MLO therefore allow one to evaluate the condensation history of air masses spanning the boundary layer and lower free troposphere. This makes

MLO an ideal location for studying boundary layer convection—and related precipitation processes—from a fixed point. Furthermore, the long history of meteorological, trace gas, and particle measurements provides a rich data context in which to evaluate the new isotopic measurements used in this analysis.

### 2.2. Water Vapor Volume Mixing Ratio and Isotope Ratio

Since October 2010, a Picarro vapor isotopic analyzer (model L1115-i) has measured the water vapor volume mixing ratio ($q$, i.e., the ratio of moles of water vapor to moles of air) and the isotope ratio in water vapor (hereafter given as $\delta^{18}O$, i.e., the deviation of the heavy-to-light oxygen isotope ratio relative to the isotope ratio of Vienna Standard Mean Ocean Water) at MLO. The analyzer samples from a hooded stack on the Charles Keeling building through 1/4 in OD stainless steel tubing maintained at room temperature, which exceeds the ambient dew point. Consequently, the instrument essentially measures the total water mixing ratio (i.e., vapor plus condensate), which must be considered during analysis even though the condensed mass is small relative to the mass of vapor. Isotopic calibrations, which are described in detail in *Bailey et al*. [2015], are performed using a LEAP Technologies PAL (Prep and Load) autosampler. For each injection sequence of a liquid standard, the first two injections are eliminated in order to minimize memory effects. Additional characterizations of the analyzer's "concentration dependence" [cf. *Lis et al*., 2008; *Sturm and Knohl*, 2010; *Johnson et al*., 2011; *Rambo et al*., 2011; *Tremoy et al*., 2011; *Aemisegger et al*., 2012; *Wen et al*., 2012; *Bailey et al*., 2013; *Steen-Larsen et al*., 2013]—which describes changes in isotope ratio caused solely by changes in the water vapor volume mixing ratio—have been obtained with a syringe-pump system. The raw $q$ measurements are not adjusted, since their bias is less than 0.33 mmol/mol compared with the volume mixing ratios estimated from regular MLO meteorological observations.

Three years of the MLO isotopic record, spanning October 2010–September 2013, were selected. Data were first converted to 15 min mass-weighted averages before calibration corrections were applied. Using both the autosampler and syringe-pump calibration points, isotope ratio observations were simultaneously corrected for their concentration dependence and for deviations from the Vienna Standard Mean Ocean Water–Standard Light Antarctic Precipitation scale. This one-step correction was accomplished using a locally weighted 2° polynomial regression (with a smoothing parameter of 0.5) [cf. *Bailey et al*., 2013]. However, because statistical fitting choices can significantly affect the accuracy of bias corrections [*Bailey et al*., 2015], a series of sensitivity tests was performed prior to choosing this particular approach. As described in the supporting information, uncertainties based on calibration choices have only a minor influence on the characterization of high and low precipitation efficiency near Hawaii: the conclusions of this analysis are therefore insensitive to the statistical fitting choices considered.

To characterize both the strength and precipitation efficiency of convective activity on the Big Island (see sections 2.3 and 2.4 below), peak values of $q$ ($q_{peak}$) and $\delta^{18}O$ ($\delta^{18}O_{peak}$) were calculated for each day. By taking observations made between 12:00 Hawaii standard time (HST) and 18:00 HST at MLO, the daily peaks in $q$ and $\delta^{18}O$ were estimated by averaging those measurements whose values were within 10% of the daily maxima of both variables. Such an approach was considered more robust than simply taking the maximum values of $q$ and $\delta^{18}O$ observed. $q_{peak}$ and $\delta^{18}O_{peak}$ values were calculated for 1056 days during the 3 year experiment (total days = 1096; the instrument did not sample ambient data on the remaining 40 days due to calibrations and maintenance). Mean nighttime $q$ and $\delta^{18}O$ values ($q_{night}$, $\delta^{18}O_{night}$), which are used to gauge background free tropospheric conditions, were calculated from observations taken between midnight and 06:00 HST.

### 2.3. Strong and Weak Convective Boundary Layer Growth

As the boundary layer grows with daytime convection on the Big Island, moisture is lofted through buoyant forcing [e.g., *Kleissl et al*., 2007] and mixed upward by trade wind cumuli. This convective mixing causes water vapor volume mixing ratios to increase at MLO during the late morning and early afternoon. (Although diabatic heating of the landmass no doubt enhances boundary layer growth compared to the surrounding marine environment, the diurnal evolution of moisture profiles on and off island is similar, suggesting that the same processes are at work [*Mendonca and Iwaoka*, 1969]). Water vapor volume mixing ratios then decrease as convection shuts down and the convective boundary layer (CBL) collapses. The stronger the convective activity is, the deeper the boundary layer grows and the more effectively moisture mixes upward. It is therefore assumed that peak daytime water vapor volume mixing ratios recorded at MLO ($q_{peak}$) should vary with the strength of CBL growth.

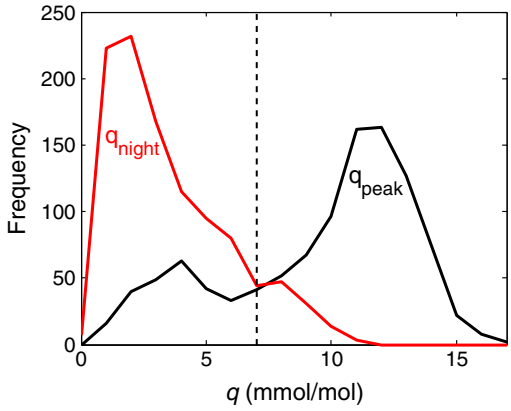


**Figure 1.** Frequency distributions of the peak daytime (black) and nighttime (red) water vapor volume mixing ratios ($q$) at MLO for the period October 2010–September 2013. Days with strong convective boundary layer growth are defined as those whose $q_{peak}$ value lies to the right of the dashed line.

As Figure 1 shows, $q_{peak}$ exhibits a bimodal distribution at MLO, with a dry mode centered around 4 mmol/mol and a larger moist mode near 11–12 mmol/mol. (While the location of the moist peak represents an average of winter and summer peaks, the bimodality is present in both seasons). The fact that the low water vapor volume mixing ratios of the dry mode are similar to nighttime values ($q_{night}$), when MLO is exposed to free tropospheric air, indicates that little, if any, boundary layer moisture reaches the height of the Observatory on these days. Consequently, the bimodality in $q_{peak}$ is used to devise an operational definition for strong and weak CBL growth: days with strong CBL growth are defined as those in which $q_{peak} > 7$ mmol/mol (i.e., moist days at MLO) and days with weak CBL growth are defined as those in which $q_{peak} \leq 7$ mmol/mol (i.e., dry days at MLO). Accordingly, 790, or 74.8%, of the measurement days are characterized by strong CBL growth at MLO.

### 2.4. Precipitation Efficiency

Previous studies suggest that the precipitation efficiency ($e = P/C$ [*Khain*, 2009]), or the ratio of the rates at which precipitation ($P$) and condensation ($C$) form, may be estimated in several ways. For example, while the ratio of the surface rain rate to the sum of vapor convergence and evaporation rates defines a bulk precipitation efficiency, it is typically the ratio of the surface rain rate to the sum of vapor condensation and deposition rates that defines the precipitation efficiency in cloud modeling studies [*Sui et al.*, 2007]. Yet depending on how these large-scale and microphysical efficiencies are estimated, they need not necessarily agree [*Sui et al.*, 2005].

Isotope ratios in water vapor offer an independent estimate of precipitation efficiency due to the fact that the removal of heavy isotopes from an ascending moist adiabatic parcel is predictable. Moreover, the condensation history of the parcel is preserved in the absence of air mass mixing, which allows one to infer cloud and precipitation processes that occurred "upstream" of the measurement location. As a result of this and the fact that boundary layer moisture is regularly transported upward with daytime convection on the Big Island, isotopic measurements made at MLO are useful for interpreting the condensation history of air parcels within the subtropical CBL.

Assuming, for example, that within a convective plume all liquid condensate is immediately converted to precipitation, the depletion of heavy isotopes can be described at any point within the atmospheric column using a simple Rayleigh distillation model [*Dansgaard*, 1964]:

$$R_i = R_0 f^{\alpha - 1}, \tag{1}$$

where $R$ is the heavy-to-light isotope ratio of an ascending parcel; $i$ is the level of observation; 0 denotes a reference level, which is here assumed to be the lifting condensation level (LCL); $f$ is the fraction of water vapor remaining at level $i$; and $\alpha$ is a temperature-dependent fractionation factor. If, in contrast, some condensate remains with the ascending parcel (i.e., $0 < e < 1$), isotopic depletion of the air mass will not be as great as equation (1) predicts and will instead follow a modified distillation model [*Dansgaard*, 1964; *Jouzel and Merlivat*, 1984; *Noone*, 2012]:

$$R_i = R_{i-1}\left(\frac{q_i + \alpha(1-e)(q_0 - q_i)}{q_{i-1} + \alpha(1-e)(q_0 - q_{i-1})}\right)^{\frac{\alpha e}{1-\alpha(1-e)}-1}, \tag{2}$$

where $q$ is the water vapor volume mixing ratio and $e$ is the precipitation efficiency. Fitting this modified model to vertical profiles of $q$ and the heavy-to-light oxygen isotope ratio ($R = {}^{18}O/{}^{16}O$), *Bailey et al.* [2013] quantitatively characterized the precipitation efficiency of the boundary layer during a 4 day field campaign on the Big Island.

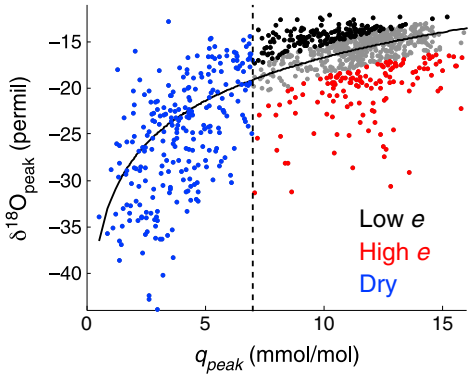


**Figure 2.** The daily peak isotope ratios ($\delta^{18}O_{peak}$) and water vapor volume mixing ratios ($q_{peak}$) for all measurement days at MLO. To characterize high and low precipitation efficiency (*e*) days, which are shown in red and black, respectively, $\delta^{18}O_{peak}$ values were regressed on $1/q_{peak}$ using a simple linear fit (solid black line). The predictions were then subtracted from the observations in order to calculate the $\delta^{18}O_{peak}$ anomaly. High *e* days are those in which convective boundary layer growth is defined as strong ($q_{peak}$ to the right of the black dashed line) and the $\delta^{18}O_{peak}$ anomaly falls below the 25th percentile, and low *e* days are those in which convective boundary layer growth is defined as strong and the $\delta^{18}O_{peak}$ anomaly exceeds the 75th percentile. Points to the left of the black dashed line (blue), which represent days of weak convective boundary layer growth, when MLO typically remains within the dry free troposphere, are not classified by precipitation efficiency. These are referred to as "dry days" in the text.

With only point measurements of isotope ratios available for the period October 2010–September 2013, and therefore no observations of $q$ or $\delta^{18}O$ at an unambiguous reference height such as the LCL, this study applies the theory behind equations (1) and (2) to devise a simpler metric for characterizing the precipitation efficiency of the subtropical CBL qualitatively. For a given $q_{peak}$, the most depleted $\delta^{18}O_{peak}$ values are assumed to be generated by processes approximating Rayleigh distillation and thus to indicate high precipitation efficiency (high *e*), while the least depleted $\delta^{18}O_{peak}$ values are assumed to indicate lower precipitation efficiency (low *e*). The validity of these assumptions will be tested as part of the analysis.

To identify anomalies in the peak daytime isotope ratio, the calibrated $\delta^{18}O_{peak}$ values were regressed on $1/q_{peak}$, using a simple linear fit, and the predicted $\delta^{18}O$ values were subtracted from the observations. Anomalies were then categorized by percentile (Figure 2). Days with strong CBL growth on which the isotopic anomaly falls below the 25th percentile are classified as high in precipitation efficiency (high *e*), while days with strong CBL growth on which the isotopic anomaly exceeds the 75th percentile are classified as low in precipitation efficiency (low *e*). No precipitation efficiency categorization is given to days with weak CBL growth since the latter are associated with dry, free tropospheric conditions at MLO (see section 2.3). Consequently, these are called "dry days" in the ensuing analysis.

Several important assumptions are involved in characterizing precipitation efficiency in this manner. The first is that the precipitation efficiency of the subtropical atmosphere near the Big Island is described by a probability distribution whose mean is neither 0 nor 1 but rather some intermediate value. As a result, regressing $\delta^{18}O_{peak}$ on $1/q_{peak}$ and subtracting the predictions from the observations ensures that the first and fourth quartiles of the $\delta^{18}O_{peak}$ anomalies expose the precipitation efficiency extremes. The second is that the variance in $q_{peak}$ is more sensitive to vertical motions than to changes in humidity either near the ocean surface or in the lower free troposphere. This assumption appears reasonable for the subtropical atmosphere near Hawaii where absolute variations in $q$ in the vertical are much larger than horizontal variations near the surface or above the trade wind inversion layer (see Figure 6 in *Bailey et al.* [2013]). Another assumption is that day-to-day variations in the flux of $\delta^{18}O$ from island evapotranspiration are small, which ensures that variations in the $\delta^{18}O_{peak}$ anomaly largely reflect changing atmospheric condensation processes. Finally, it is important to stress that while this study characterizes precipitation efficiency using point measurements at MLO, the cloud and precipitation processes described are associated with the CBL and are therefore assumed more likely than not to occur at elevations below the Observatory.

### 2.5. Synoptic Analyses

To study the large-scale conditions under which different precipitation efficiencies arise, composites of horizontal and vertical winds, geopotential height, and total column water were created for high *e*, low *e*, and dry days using the 0.75° × 0.75° European Centre for Medium-Range Weather Forecasts (ECMWF) Reanalysis ERA-Interim. The analysis was repeated using the 2.5° × 2.5° National Centers for Environmental Prediction (NCEP)–National Center for Atmospheric Research (NCAR) Reanalysis, and the results presented here are insensitive to the choice of reanalysis data. Three-dimensional back trajectories associated with

persistent high or low *e* events (i.e., periods of high or low *e* convection lasting three or more days, with no more than 1 day of separation in between) were calculated with NOAA's HYSPLIT (Hybrid Single-Particle Lagrangian Integrated Trajectory) model (http://ready.arl.noaa.gov/HYSPLIT.php), using the NCEP-NCAR Reanalysis and model vertical velocity.

### 2.6. Aerosols, Ozone, and Methane

To evaluate differences in vertical distributions of atmospheric constituents measured at MLO during high *e*, low *e*, and dry days, mean values of particle (condensation nucleus) number concentration, total light scattering coefficient ($\sigma_{sp}$), ozone concentration, and methane concentration were calculated for each hour of the diurnal cycle from NOAA-Earth System Research Laboratory data collected as part of routine long-term monitoring efforts. Recall from section 2.1 that although all data are measured in situ at MLO, the diurnal growth and collapse of the boundary layer on the Big Island creates the opportunity to sample across a substantial vertical column of the atmosphere. Particle number concentrations are measured at MLO with a TSI Model 3760 particle counter. One-minute averages of these data (P. Sheridan, personal communication, 2014) were converted to STP by assuming an instrument temperature of 12°C and a pressure of 680 hPa (resulting in a uniform scale factor of 1.555). The total scattering coefficient is measured at three wavelengths (450 nm, 550 nm, and 700 nm) with a nephelometer (TSI Model 3563). This study utilizes 1 min averages of these data (P. Sheridan, personal communication, 2014) and reports scattering measured at the 550 nm wavelength. Only those nephelometer measurements made with the normal 10 μm cut size and corrections for both STP and truncation [*Anderson and Ogren*, 1998] applied are used. Hourly methane data—measured by gas chromatography—are available by anonymous ftp to ftp://ftp.cmdl.noaa.gov/data/trace_gases/ch4/in-situ/surface/mlo/ [*Dlugokencky et al.*, 1995, 2014], and 5 min surface ozone data—measured by ultraviolet absorption photometer—are available by anonymous ftp to ftp://ftp.cmdl.noaa.gov/ozwv/SurfaceOzone/MLO/ [*McClure-Begley et al.*, 2014].

### 2.7. Mixing Model

To evaluate differences in the relative importance of dynamical and microphysical controls on vertical distributions of atmospheric constituents measured at MLO during high and low *e* days, a column model was constructed that approximates vertical motions associated with daytime convective boundary layer growth on the Big Island of Hawaii. Within the model, vertical mixing, which presumably results from CBL growth, is expressed as nonlocal entrainment into a transition layer between the Hawaiian boundary layer and free troposphere. *Bailey et al.* [2013] found that transition layers regularly develop above the base of the trade wind inversion and are a key feature of vertical water vapor distributions. The model assumes that early in the day, as the CBL deepens, turbulent eddies dominate vertical motions and mix boundary layer constituents into the transition layer. Later in the day, as the boundary layer collapses, the downward mixing of free tropospheric air into the transition layer is assumed to dominate. It is during this time that downslope winds replace upslope winds on the Big Island [*Garrett*, 1980]. For the sake of clarity, these two cases are referred to as upward and downward mixing.

The mass balance of the column for $q$ is

$$\frac{\partial q}{\partial t} = w_{up} m(q_{BL} - q) + w_{down} m(q_{FT} - q), \tag{3}$$

where $q_{BL}$ is the initial boundary layer value of the water vapor volume mixing ratio, $q_{FT}$ is a value chosen from nighttime observations to represent the free troposphere, $m$ is the mixing coefficient, and $w_{up}$ and $w_{down}$ are the weighting functions that control whether mixing of boundary layer air upward or free tropospheric air downward dominates, respectively. Weights are set to either zero or one within the boundary layer and free troposphere, depending on the time of day, and are allowed to vary linearly between zero and one as a function of time and height across the transition layer in order to approximate the *erf* function, which appears in the analytical solution to the diffusion equation expressed in equation (3) [e.g., *Noone et al.*, 2011] (see Appendix A for equations governing $w_{up}$ and $w_{down}$). An example of the upward weighting function and its effect on the modeled $q$ profile is shown in Figure S1 in the supporting information.

Three parameters are used to set the weighting functions: the times at which upward mixing starts ($t_{up,start}$) and peaks ($t_{up,peak}$) and the height to which the transition layer—defined as the region of mixed boundary layer and free tropospheric air—grows ($z_{trans}$) (see Appendix A). The following parameter values were considered: upward mixing start times were examined for every hour between 0 and 3 h past model initiation,

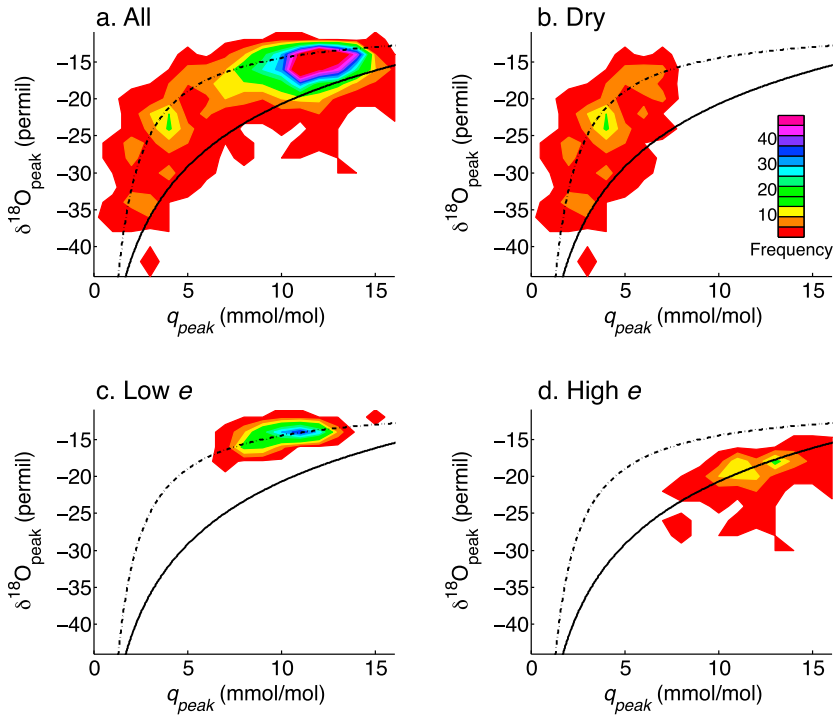


**Figure 3.** Bivariate frequency distributions of MLO $q_{peak}$ and $\delta^{18}O_{peak}$ for (a) all days during the 3 year measurement campaign; (b) dry days, when boundary layer air masses fail to reach the height of the Observatory; (c) low precipitation efficiency days; and (d) high precipitation efficiency days. Hypothetical mixing (dashed) and saturated Rayleigh distillation (solid) lines for Hawaii are calculated independently, assuming an air mass of oceanic origin whose $\delta^{18}O$ equals −12‰ [cf. *Galewsky et al.*, 2007; *Bailey et al.*, 2013] and whose $q$ value equals the mean water vapor volume mixing ratio at the LCL (i.e., ~22 mmol/mol, according to Hilo radiosondes for the field campaign period). The dry end-member for the mixing line is constrained by the cluster of $\delta^{18}O_{night}$ and $q_{night}$ values observed at MLO (not shown).

upward mixing peak times were examined for every hour between 4 and 9 h past model initiation, mixing coefficients were examined every 0.1 $h^{-1}$ between 0.2 and 1.5 $h^{-1}$, and transition layer heights were examined every 100 m between 3400 m (the height of MLO) and 4000 m (the top of the model). The best choice for each of these parameters was selected by minimizing the root-mean-square error (RMSE) between model output and $q$ observations—averaged to each hour of the day—for high and low precipitation efficiency days separately. These optimal values were then used to model diurnal patterns in other trace gases, including the $H_2{}^{18}O$ concentration (which was later converted to $\delta^{18}O$), and particle number concentration, with only the initial boundary layer value varying for each constituent. The best fit parameters are discussed in section 3.4.

The model is discretized at 79 levels in the vertical, spanning 100–4000 m and spaced 50 m apart. The top of the boundary layer is set at 2000 m, which is within the range of heights at which *Ridley et al.* [1997] observed the trade wind temperature inversion by aircraft. At model initiation, heights spanning 100 to 2000 m are assigned the initial boundary layer $q$ value ($q_{BL}$), while heights above are assigned the free tropospheric value ($q_{FT}$) estimated from nighttime observations. The model time step is 36 s.

## 3. Results

### 3.1. Characterizing Precipitation Efficiency

Using the $\delta^{18}O_{peak}$ anomalies to characterize precipitation efficiency at MLO, 180 days (22.8% of days during which CBL growth is strong) are classified as having low precipitation efficiency (low $e$) and 146 days (18.5% of days during which CBL growth is strong) as having high precipitation efficiency (high $e$). Figure 3 illustrates the bivariate distributions in $q_{peak}$ and $\delta^{18}O_{peak}$ associated with these two classifications. Bivariate distributions for all measurement days and dry (i.e., weak CBL growth) days are also shown for comparison. Although the

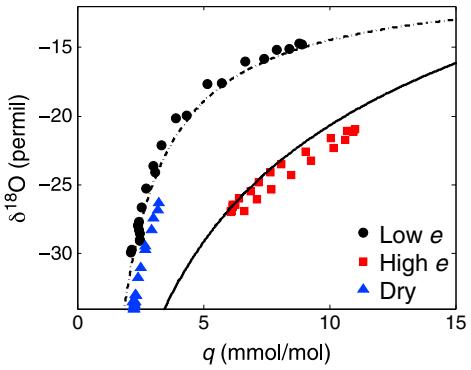


**Figure 4.** The bivariate evolution of $q$ and $\delta^{18}O$ for low precipitation efficiency days (black circles), high precipitation efficiency days (red squares), and dry days (blue triangles). The symbols represent 3 year means for each hour of the day. The solid line represents a hypothetical saturated Rayleigh distillation process, while the dashed line represents idealized mixing between the subtropical boundary layer and free troposphere (see Figure 3 for calculation details).

precipitation efficiency classification is based on a single pair of points from each day, rather than estimated quantitatively using equation (2), the data nevertheless cluster around lines derived from isotopic theory, which are designed to model processes that influence the vertical profile of the subtropical atmosphere. The $q_{peak}$ and $\delta^{18}O_{peak}$ values for high $e$ days, for instance, cluster along the hypothetical Rayleigh distillation line predicted by equation (1) (see Figure 3 caption for more details). Since the Rayleigh model assumes that all condensate is immediately removed as precipitation, isotopic observations following such a distillation are consistent with maximal precipitation efficiency ($e = 1$). Meanwhile, the peak values for low $e$ days cluster around a hypothetical mixing line, estimated from near-surface and free tropospheric values typical of the Hawaiian region. When no precipitation occurs ($e = 0$), both the isotope ratio and total water mixing ratio of an air parcel will be conserved, unless the air mass mixes with another. It is thus reasonable to expect that low precipitation efficiency convection near Hawaii would resemble a mixing process in which water vapor and cloud condensate are exchanged between the saturated boundary layer and the dry subtropical free troposphere. The same mixing line might, of course, also describe the exchange of moisture between two unsaturated air masses in the vertical; however, differentiating among these cases is not critical for the purposes of this study, given that ventilation of moisture from the boundary layer to the free troposphere would occur regardless.

The clustering of the $q_{peak}$ and $\delta^{18}O_{peak}$ values around the Rayleigh and mixing lines thus suggests that the qualitative characterization of precipitation efficiency described in section 2.4 is indeed physically representative. Figure 4 lends additional support to this claim by showing 3 year means in MLO $q$ and $\delta^{18}O$ calculated for each hour of the diurnal cycle on high and low precipitation efficiency days. Since these hourly means essentially represent vertical covariations in $q$ and $\delta^{18}O$, due to the cyclic nature of boundary layer growth and collapse on the Big Island, one can conclude that the average atmospheric profile when $e$ is high follows a Rayleigh distillation (solid line) while the average profile when $e$ is low follows a mixing (dashed) line.

### 3.2. Large-Scale Controls on MLO Convection

While the Hawaiian Islands are located within or very near the perennial subtropical high, differences in large-scale circulation are nevertheless apparent when we distinguish among low $e$, high $e$, and dry days at MLO. Figure 5 shows composites from the ECMWF Reanalysis ERA-Interim of jet-level winds, total column water (TCW), and surface-level wind and pressure fields for these three cases. Figure 6 shows the same variables as anomalies from the 3 year mean.

On days in which the precipitation efficiency is defined as low, a branching of the midlatitude jet occurs, creating a westward retraction and strengthening of 200 hPa winds near Hawaii (Figures 5b and 6b). This pattern is stronger during winter (December-January-February (DJF)) than other seasons (seasonal composites are not shown). Near the jet exit region, a low-pressure anomaly forms at the surface (~45°N, 150°W) (Figure 6h), which forces the subtropical high eastward (Figure 5h). Anticyclonic flow around the high-pressure region directs easterly (low-level) winds toward Hawaii. With the strengthening of the westerlies aloft, wind shear—defined as the magnitude of the vector difference between the 850 hPa and 200 hPa levels [*DeMaria and Kaplan*, 1994]—is enhanced, and this likely facilitates convective activity over the Big Island. Indeed, wind shear is significantly stronger at the 95% confidence level for low $e$ days ($5.7 \times 10^{-3}\,s^{-1}$) than for high $e$ days ($4.8 \times 10^{-3}\,s^{-1}$) or dry days ($5.1 \times 10^{-3}\,s^{-1}$). Nevertheless, the atmospheric column is relatively dry (Figures 5e and 6e), which is consistent with the idea that ageostrophic flow near jet exit regions allows dry midlatitude air to descend into the subtropics [*Cau et al.*, 2007]. The mixing of a moist convective boundary layer with

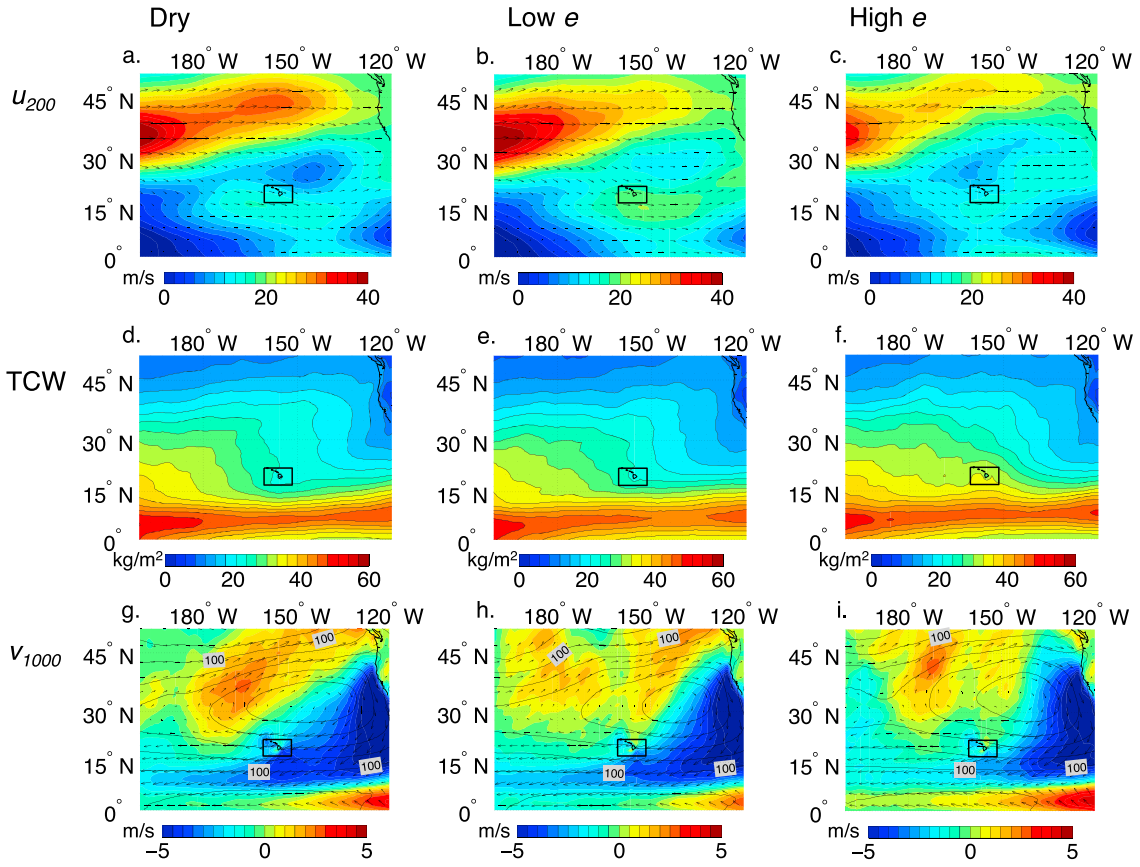


**Figure 5.** October 2010–September 2013 composites of (a–c) 200 hPa zonal winds, with mean 200 hPa wind vectors represented by arrows; (d–f) total column water (TCW); and (g–i) 1000 hPa meridional winds, with mean 1000 hPa wind vectors represented by arrows. The black contours in Figures 5g–5i represent mean 1000 hPa geopotential heights, and the 100 m contour is labeled. Contours are every 20 m. From left to right, columns represent dry days, low precipitation efficiency days, and high precipitation efficiency days. In each panel, the black rectangle is centered on Mauna Loa Observatory.

a drier-than-normal free troposphere, in turn, likely promotes cloud evaporation and limits precipitation, as expected for the low *e* categorization.

When the precipitation efficiency is defined as high, there is little anomalous activity at the jet level (Figure 6c). Instead, the surface high shifts northward (Figure 5i), weakening the anticyclonic circulation that typically transports dehydrated air from the eastern Pacific toward Hawaii. As a result, more tropical air is able to move northeast toward the islands (Figure 6i), and an overall moistening of the atmospheric column occurs (Figures 5f and 6f). This pattern, like the jet-level anomaly pattern associated with low *e* days, is stronger in winter (DJF) than during other seasons.

Dry days, in contrast, show both a strengthening and northward shift of the midlatitude jet (Figures 5a and 6a) and the formation of a surface high-pressure anomaly over the Hawaiian Islands (Figure 6g). As a result of the pressure anomaly, MLO experiences enhanced subsidence, which suppresses convection, as well as enhanced northeasterly flow, which transports dehydrated air masses from the eastern Pacific. Dry days are, consequently, also associated with a drier-than-normal atmospheric column (Figures 5d and 6d).

Ensemble back trajectories associated with persistent high and low *e* events (i.e., periods of high or low *e* convection lasting three or more days, with no more than 1 day of separation in between) further illustrate the differences between high and low precipitation efficiency days at MLO (Figure 7). Air masses associated with high precipitation efficiency events are more likely to have originated at lower latitudes and to have come from the southeast, in particular. This finding supports the previous conclusion that as anticyclonic circulation in the vicinity of Hawaii weakens, moisture-laden air masses from the tropics are more likely to extend northward. In contrast, for low precipitation efficiency events, MLO air masses are more likely to have

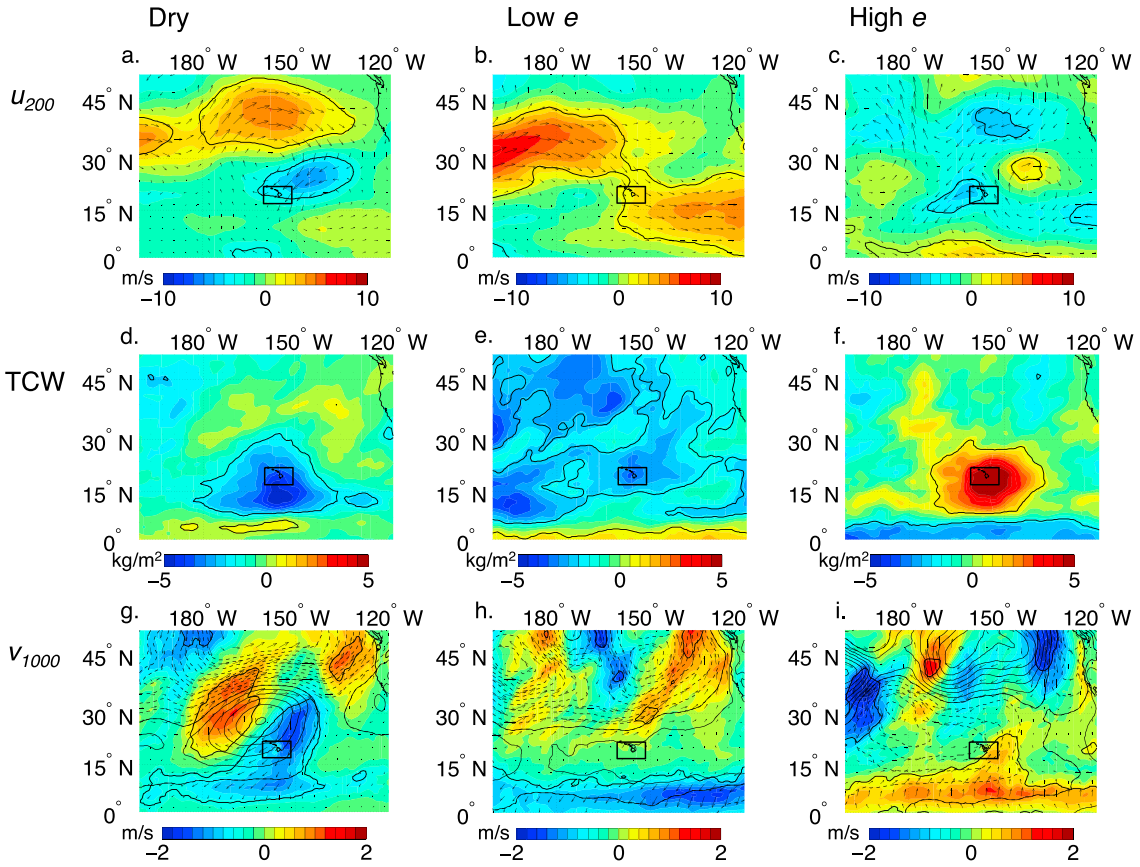


**Figure 6.** Anomalies of (a–c) 200 hPa zonal winds and wind vectors (arrows), (d–f) total column water (TCW), and (g–i) 1000 hPa meridional winds and wind vectors (arrows) for dry, low precipitation efficiency, and high precipitation efficiency days (left to right). Anomalies are calculated as differences between the composites for each type of convective classification and the October 2010–September 2013 mean. Anomalies that are significant at the 95% confidence level are outlined in black. The black contours in Figures 6g–6i represent anomalies in 1000 hPa geopotential heights, with positive contours solid and negative contours dashed. Contours are every 2 m. In each panel, the black rectangle is centered on Mauna Loa Observatory.

traveled from the northwest, originating from as far away as the Asian continent. These air masses presumably cross the Pacific following the enhanced southern branch of the jet stream depicted in Figures 5b and 6b.

Although one would expect water vapor in higher-latitude air masses to be more depleted than water vapor in lower-latitude air masses due to the temperature dependence of isotopic fractionation, the MLO observations reveal higher daytime isotope ratios associated with Figure 7a, which depicts numerous northwesterly trajectories. Consequently, local mixing and microphysical processes—which determine how much condensate is removed as rain—appear to be more influential in determining the peak water vapor isotope ratio near Hawaii than the zonal origin of the air mass.

### 3.3. Convective Transport of Atmospheric Constituents

While variations in transport pathways, brought about by differences in large-scale circulation patterns, may influence the concentrations of atmospheric constituents at MLO, differences in the strength of convective mixing and microphysical processes may also play an important role. To evaluate the relative importance of these large-scale and local processes in regulating vertical distributions of atmospheric constituents during different precipitation efficiency days, we examine the diurnal cycles of seven variables measured at MLO: $q$, $\delta^{18}O$, precipitation, particle number concentration, aerosol scattering coefficient (550 nm), ozone, and methane. Figure 8 shows 3 year means of each of these variables for each hour of the day during high $e$, low $e$, and dry days.

Dry days, when MLO largely remains in the free troposphere, serve as a helpful reference for variations in atmospheric constituents observed during high and low $e$ days. As expected, they show the least variation in all seven

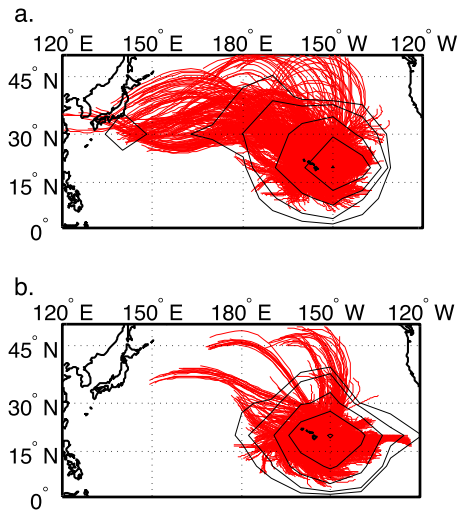


**Figure 7.** Three-day ensemble back trajectories calculated from the NOAA HYSPLIT model, using the NCEP-NCAR Reanalysis, for air masses arriving at Mauna Loa Observatory during (a) low or (b) high precipitation efficiency events (see text). Contours estimate the probability density of air mass source regions by marking the 10° × 10° grid boxes in which 1%, 2%, 5%, 10%, or 20% of the trajectory end points lie.

variables and are characterized by very low values in $q$, $\delta^{18}O$, and particle number concentration. Relatively high ozone values, meanwhile, confirm that the Observatory lies within the free troposphere on these days and support the interpretation that CBL growth is too weak to transport boundary layer moisture to the elevation of MLO. Yet although convection is weak, Figure 8b indicates that some vertical motions occur. Indeed, while $q$ and ozone are nearly constant throughout the 24 h period, the isotope ratio increases during the afternoon.

Of course, another possibility is that this increase is driven not by vertical motions but by land-atmosphere exchange. Vegetation likely participates in the atmospheric hydrology of the Big Island by reevaporating intercepted rain or by transpiring rain recently fallen on the shallow organic soils that cover the igneous bedrock. However, while such processes could drive diurnal variations in the isotope ratio of the boundary layer, the magnitude of these variations would be small relative to the variance in isotopic observations at MLO. In addition, since the arid lava fields at higher elevations are largely devoid of vegetation, evapotranspiration rates near the Observatory are very low. Therefore, it is more likely that diurnal variations in $\delta^{18}O$ demonstrate the isotope ratio's efficacy in tracing free tropospheric air masses.

During high and low $e$ days, much higher values of $q$, $\delta^{18}O$, and particle number concentration are observed, and large differences between nighttime and daytime concentrations indicate a clear transition from free tropospheric to boundary layer air. As shown in Figure 8a, the large diurnal variations in water vapor volume mixing ratio for low precipitation efficiency days signify a substantial jump in $q$ between a relatively moist boundary layer and very dry free troposphere. Mixing between such air masses would dehydrate the boundary layer and limit precipitation throughout the atmospheric column. It is therefore no surprise that, on average, precipitation is zero at MLO on low $e$ days (Figure 8c). In contrast, when $e$ is high, measurable precipitation is evident, and elevated $q$ during both day and night suggests sustained convective activity. Small variations in isotope ratio support this claim (Figure 8b): *Noone et al.* [2011] observed similar isotopic enrichment over the course of several nights when a tropical plume crossed the Hawaiian Islands and generated heavy precipitation.

Absolute differences in nighttime isotope ratios among high $e$, low $e$, and dry days (Figure 8b) are consistent with the different large-scale circulation patterns and transport pathways identified in section 3.2. High precipitation efficiency nights, which are often influenced by tropical moisture, exhibit the highest isotope ratios. Meanwhile dry nights—during which enhanced anticyclonic circulation channels dry and depleted eastern Pacific air toward the islands—exhibit the lowest isotope ratios. Low $e$ nights are more depleted than high $e$ nights, due to the fact that low $e$ air masses often originate north of Hawaii. However, they are less depleted than dry nights since low $e$ air masses are more likely to have traveled directly from the comparatively enriched western Pacific, instead of undergoing extensive mixing with even higher-latitude air masses.

Similar conclusions may be drawn from the diurnal plots of ozone and methane (Figures 8f and 8g). Concentrations of both trace gases are lowest for high $e$ days, consistent with relatively clean tropical outflow. In contrast, they are highest for low $e$ days, when enhanced westerly winds are able to transport pollutants from the Asian continent toward the Hawaiian Islands. Other studies based at MLO have likewise observed high methane or ozone concentrations with westerly or northerly trajectories and low concentrations with southerly trajectories [*Harris et al.*, 1992; *Oltmans et al.*, 1996; *Ridley et al.*, 1997; *Lin et al.*, 2014]. Ozone and methane thus clearly reflect the distinct transport pathways created by the large-scale circulation differences observed.

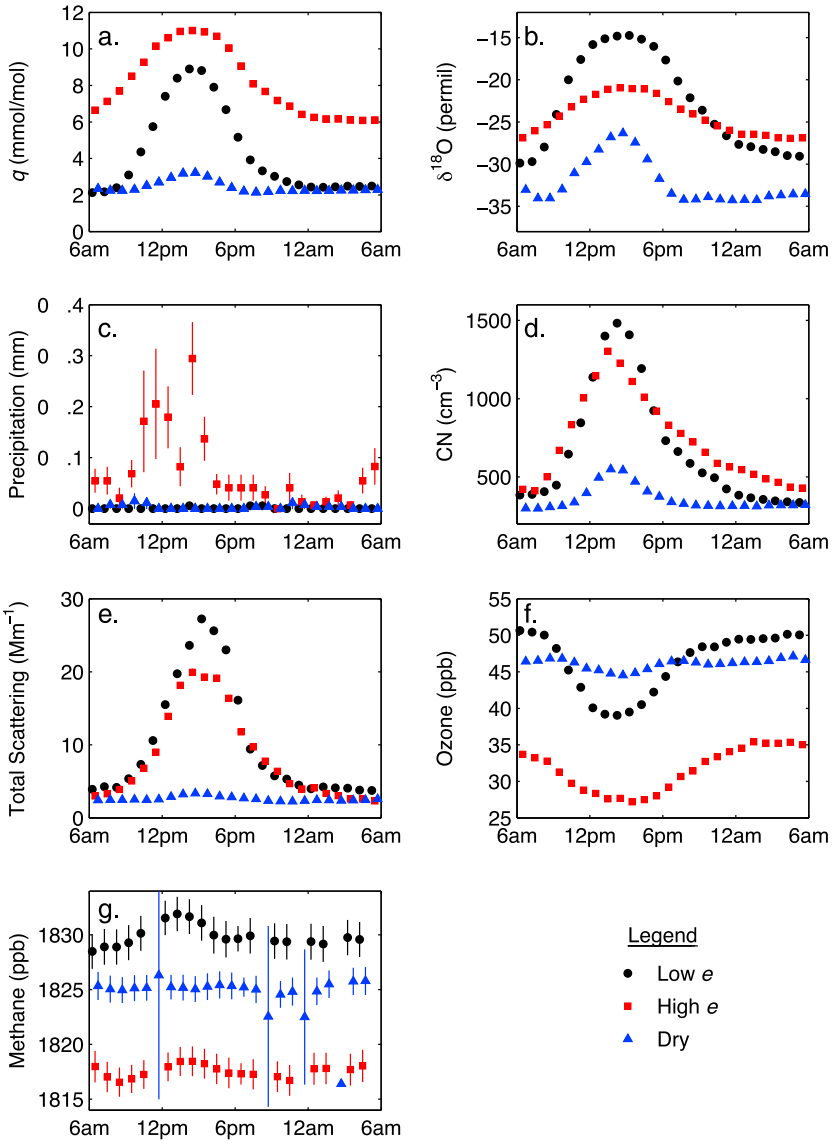


**Figure 8.** Three-year means for each hour of the day representing diurnal cycles for low precipitation efficiency (black circles), high precipitation efficiency (red squares), and dry days (blue triangles) at MLO. Diurnal cycles are shown for the following variables: (a) the water vapor volume mixing ratio ($q$), (b) the isotope ratio ($\delta^{18}O$), (c) precipitation, (d) condensation nucleus (CN) concentration, (e) aerosol total scattering coefficient, (f) ozone, and (g) methane. Standard errors for each mean are represented by vertical lines; however, in many cases, the symbols are larger than the errors.

Aerosol properties, in contrast, are quite similar among the three convective cases at night but exhibit stark differences during the day. Figures 8d and 8e, for instance, indicate lower particle concentrations and less scattering during the afternoons of high $e$ days compared with low $e$ days. One possible explanation for this observation, which is supported by the MLO precipitation patterns (Figure 8c), is that aerosols are effectively scavenged from the boundary layer during higher precipitation efficiency conditions. Such findings would support the hypothesis that precipitation processes are more important than proximity to the emission source in controlling number concentrations of particulates [*Wood et al.*, 2012]. A second possibility is that these differences in aerosol properties reflect differences in boundary layer growth: were the boundary layer and/or transition layer to remain elevated throughout a high $e$ diurnal cycle but peak at a lower altitude than on a low $e$ day, this could explain the diurnal patterns in number concentrations observed. Both of these scenarios are explored in section 3.4 below.

**Table 1.** Best Parameters for Modeling High and Low Precipitation Efficiency (*e*) Days[a]

| | Low *e* | High *e* |
|---|---|---|
| $m$ | 0.7 $h^{-1}$ | 0.6 $h^{-1}$ |
| $t_{up,start}$ | 07:00 HST | 06:00 HST |
| $t_{up,peak}$ | 12:00 HST | 10:00 HST |
| $z_{trans}$ | 3700 m | 3500 m |
| $q_{BL}$ | 16 mmol/mol | 22 mmol/mol |
| $q_{FT}$ | 2 mmol/mol | 6.5 mmol/mol |
| $\delta^{18}O_{BL}$ | −13‰ | −17‰ |
| $\delta^{18}O_{FT}$ | −30‰ | −27‰ |
| $O_{3BL}$ | 27 ppb | 14 ppb |
| $O_{3FT}$ | 50 ppb | 33 ppb |
| $CN_{BL}$ | 2400 $cm^{-3}$ | 3100 $cm^{-3}$ |
| $CN_{FT}$ | 380 $cm^{-3}$ | 380 $cm^{-3}$ |

[a] $m$ = mixing coefficient, $t_{up,start}$ = start of upward mixing, $t_{up,peak}$ = peak of upward mixing, $z_{trans}$ = height at the top of the transition layer, BL = initial concentration of the boundary layer, FT = initial concentration of the free troposphere, $q$ = water vapor volume mixing ratio, and CN = condensation nucleus concentration.

### 3.4. Modeling Mixing for Different Precipitation Efficiencies

To better evaluate the role of microphysical processes in influencing aerosols at MLO, we consider whether the mixing model, described by equation (3), can explain the essential features of diurnal variations in particle number concentrations observed. It is assumed that if vertical mixing can replicate the diurnal patterns for both high and low *e* days, then precipitation scavenging and other microphysical processes are likely negligible. If, on the other hand, mixing can replicate the pattern on low *e* days but not high *e* days, it can be inferred that microphysical processes contribute to differences between these two cases.

As described in section 2.7, a column model—in which the initial boundary layer value, the times marking the start and peak of upward mixing, the mixing coefficient, and the height of the transition layer are allowed to vary—was constructed to simulate diurnal patterns in MLO tracer concentrations. Optimal values for the last four free parameters were selected by fitting the model to the $q$ observations and the model independently evaluated by replicating the observed diurnal variations in $\delta^{18}O$ and ozone. For each atmospheric constituent modeled, initial boundary layer values were selected by reducing the RMSE between the hourly averaged model output and the corresponding observed diurnal pattern. Initial free tropospheric values were set to the nighttime values observed. The best fit parameters for high and low precipitation efficiency days for all modeled tracers ($q$, $\delta^{18}O$, ozone, and particle number concentration) are listed in Table 1.

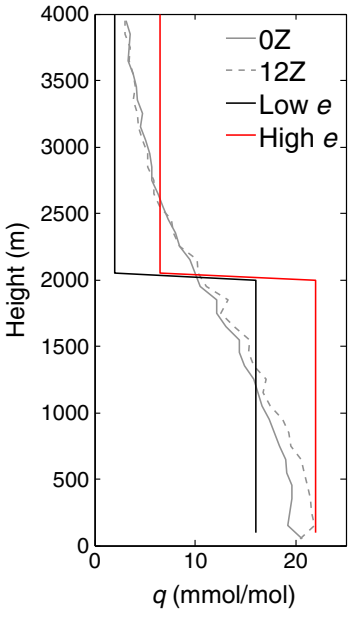


**Figure 9.** Initial water vapor volume mixing ratio ($q$) profiles used to model vertical mixing during high (red) and low (black) precipitation efficiency days compared with mean 00:00 Z (solid gray) and 12:00 Z (dashed gray) $q$ profiles derived from Hilo, Hawaii, upper air radiosondes for October 2010–September 2013.

Although precipitation processes will reduce $q$ so that it no longer serves as a conserved tracer in the strictest sense, such reductions should be negligible compared to the hourly changes brought about by vertical motions near Hawaii. The $q$ observations should thus effectively track boundary layer growth during both high and low precipitation efficiency days, and several findings support this interpretation. First, comparison of the initial model $q$ with mean profiles derived from Hilo radiosondes for October 2010–September 2013 (available at http://weather.uwyo.edu/upperair/sounding.html) suggests that the model initiation for both high and low *e* days is physically reasonable (Figure 9). Second, ozone, unlike the moisture variables or particle number concentrations, will not be removed from the atmosphere by precipitation processes. Therefore, the model's ability to reproduce ozone patterns for both high and low *e* days (Figure 10c) suggests that the relevant processes are adequately resolved for characterizing vertical motions near Hawaii.

As indicated by Figure 10, the column mixing model readily explains the diurnal variations in $q$, $\delta^{18}O$, and ozone observed during both high and low precipitation efficiency days. (As with $q$, large variations in $\delta^{18}O$ across the diurnal cycle will first and foremost

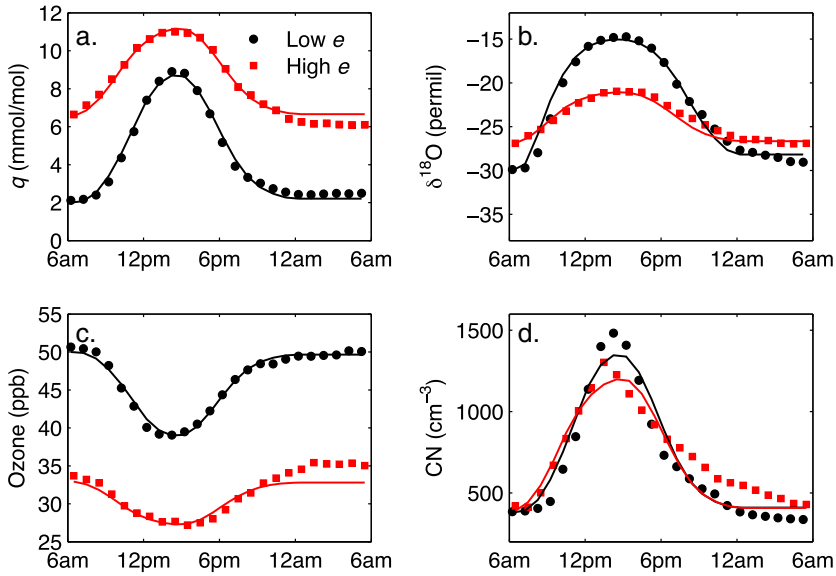


**Figure 10.** Observed and modeled diurnal cycles for (a) the water vapor volume mixing ratio ($q$), (b) the isotope ratio ($\delta^{18}$O), (c), ozone, and (d) condensation nucleus (CN) concentration on high (red) and low (black) precipitation efficiency days at MLO. The lines represent the results from the single-column mixing model.

reflect the transition from free troposphere to boundary layer and back. Any influence of evapotranspiration on the $\delta^{18}$O diurnal cycle is neglected). While CBL growth on low $e$ days begins later than on high $e$ days, the mixing coefficient is higher and the transition layer is deeper (Table 1). Thus, even though the atmospheric column is drier, vertical transport of atmospheric constituents is slightly stronger for a period of time.

These findings suggest that differences in transition layer depth could be partially responsible for differences in particle number concentrations between high and low $e$ days. However, while the mixing model replicates many qualitative and quantitative features of the aerosol diurnal cycle on low $e$ days, it cannot reproduce the observed diurnal pattern in particle number on high $e$ days (Figure 10d), indicating that microphysical processes are also at work. Since there is little or no precipitation when $e$ is low, convective transport should indeed be the principal process regulating MLO number concentrations during these times. Nevertheless, particle nucleation and growth—which are not included in the model formulation—may amplify the boundary layer concentrations observed in the early afternoon. For this reason, the model may underestimate the peak number concentration on low $e$ days. In contrast, on high $e$ days, differences between model and observations are much larger. The observed particle number concentration peaks at 13:00 HST, well before the predicted peak at 15:00 HST, and then declines slowly throughout the afternoon and evening. The model, meanwhile, follows a steeper hyperbolic curve. These discrepancies lead us to speculate that boundary layer particles are scavenged before CBL air masses reach MLO near midday, while new particles are produced at altitudes above the Observatory, presumably from local volcanic emissions of sulfur dioxide that have mixed into the transition layer and free troposphere. These new particles would create the appearance of higher-than-expected number concentrations at MLO at night, once the boundary layer collapses and the Observatory is once again exposed to the free troposphere. Together, these findings provide evidence that microphysical processes are particularly important in shaping vertical distributions of aerosols on high $e$ days.

Finally, while it is possible to reproduce diurnal patterns in $q$, $\delta^{18}$O, and ozone by treating the top of the boundary layer as a material surface that moves up and down over the course of the day, this is only the case so long as a transition layer—in which mixing between the boundary layer and free troposphere has previously occurred—is included in the initial tracer profile. Consequently, not all of the vertical mixing influencing the diurnal patterns discussed need have occurred on a single day; mixing may have occurred over the course of several days.

## 4. Discussion

This study has used isotope ratios in water vapor to characterize the precipitation efficiency ($e$) of boundary layer convection on the Big Island of Hawaii and to examine how large-scale circulation, vertical mixing

processes, and microphysics vary between high and low precipitation efficiency days. Isotopic tracers, with their sensitivity to water phase changes, create unique opportunities to study the condensation and precipitation history of air masses; however, mixing processes can obfuscate this microphysical record. In characterizing the precipitation efficiency using the daily peak $q$ and $\delta^{18}O$ values observed at Mauna Loa Observatory (MLO), this study has assumed that the vertical mixing needed to deepen the boundary layer and transport moisture upward does not erase the isotopic profile set by clouds and precipitation downslope. It has also assumed that a single precipitation efficiency value is representative of the atmospheric column sampled at MLO on a given day. In so doing, the study offers an integrated perspective on microphysical processes, which likely exhibit spatial and temporal heterogeneity near the Big Island [cf. *Bailey et al*., 2013].

Nevertheless, the results suggest that these assumptions are reasonable for evaluating bulk differences between high and low precipitation efficiency convection. For example, as expected, the mean atmospheric profile associated with high $e$ days at MLO resembles a Rayleigh distillation, which describes the isotopic depletion of a moist convective plume when $e \approx 1$. When $e$ is low, the mean atmospheric profile is consistent with a mixing process, such as might occur when trade wind cumuli near Hawaii detrain into the dry subtropical free troposphere rather than precipitate. Composites of large-scale circulation patterns provide further evidence of the physical robustness of the precipitation efficiency characterization due to the links between cloud systems and dynamical features.

The analysis shows that while high $e$ days are associated with a weakening of anticyclonic circulation that allows moist tropical air to reach the Hawaiian Islands, low $e$ days are associated with strengthened westerly flow and enhanced wind shear. These results are consistent with model studies of deep convection by *Ferrier et al.* [1996], which found higher precipitation efficiency where atmospheric moistening was greater and upshear convection reduced. Moreover, *Elison Timm et al.* [2013] found that heavy rain events over Hawaii are associated with southerly moisture transport, which resembles the high $e$ low-level circulation pattern described here.

Differences in trace gas concentrations between circulation patterns are also consistent with what previous studies report. Several papers, for example, have studied the westerly transport pathway [*Harris and Kahl*, 1990; *Merrill et al*., 1989; *Ridley et al*., 1997], which is found here to be associated with low $e$ and higher concentrations of ozone and methane. Westerlies not only transport high concentrations of trace gases and particles from Eurasia [*Harris et al*., 1992; *Ridley et al*., 1997; *Perry et al*., 1999] but they also tend to occur more frequently in winter, when emissions of pollutants like methane are higher [*Harris et al*., 1992]. In addition, cyclonic variability associated with enhanced jet flow may encourage stratosphere-troposphere exchange, which has been linked to high ozone near Hawaii [*Oltmans et al*., 2004]. Importantly, if the circulation patterns that channel westerly flow change in frequency, either as a result of climate forcing or decadal climate variability, as recent work suggests has already occurred [*Oltmans et al*., 2006; *Lin et al*., 2014], this paper's findings indicate that the frequency of low precipitation efficiency convection will change as well. Moreover, since the position of the subtropical high—a well-resolved climate model feature—appears to be a distinguishing characteristic of the circulation patterns identified, future work might effectively use general circulation model simulations to test how the frequency of high and low precipitation efficiency days near Hawaii will change with future warming.

Despite clear differences in methane and ozone concentrations between high and low precipitation efficiency days, background (i.e., nighttime) particle number concentrations and aerosol scattering were quite similar. This is not surprising: previous research suggests that high particle and trace gas concentrations do not always coincide [*Ridley et al*., 1997]. Indeed, while westerly flow often transports high ozone concentrations toward Hawaii, cloud and precipitation processes may wash out aerosols en route. Similarly, low-ozone air from the tropics may be characterized by higher-than-expected particle number concentrations due to recent vertical mixing between boundary layer and free tropospheric air. Thus, both convective mixing and microphysical processes can obfuscate the expected positive correlation between trace gas and particulate concentrations, which highlights the value of the isotopic measurements in distinguishing these processes.

Convective mixing and microphysical processes also appear to regulate *daytime* particle number concentrations at MLO, with microphysical processes more influential on high $e$ days. As discussed by *Clarke* [1993] and *Nilsson et al.* [2001], scavenging of aerosol—for example by clouds and precipitation—reduces the condensation sink for particle-forming gases like $H_2SO_4$, which can ultimately facilitate particle nucleation. Scavenging could therefore explain the unexpected decline in particle number on high $e$ days, while

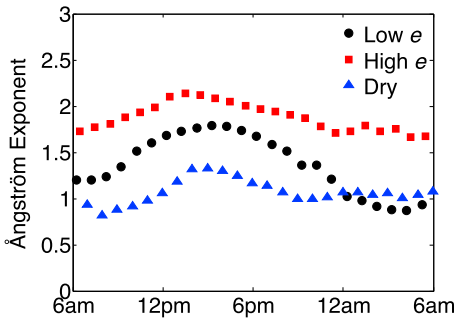


**Figure 11.** The Ångström exponent on low precipitation efficiency days (black circles), high precipitation efficiency days (red squares), and dry days (blue triangles), calculated from 3 year means in the total scattering coefficient at three wavelengths for each hour of the diurnal cycle.

subsequent nucleation could account for the higher-than-expected concentrations observed later during the evening. The fact that the total scattering coefficient—which is more sensitive to large particles—is symmetrical about the midday peak on both high and low *e* days (Figure 8e) supports the hypothesis that recently nucleated particles contribute to the differences in number concentration between high and low precipitation efficiency convection. Nucleation may also be enhanced by lofting of precursor gases [*Nilsson et al*., 2001]—a mechanism that may be particularly effective in forming sulfate particles over volcanic islands like Hawaii [*Thornton et al*., 1997]—or by increases in environmental relative humidity brought about by convective activity [*Hegg et al*., 1990; *Perry and Hobbs*, 1994].

Disparities in particle size provide further evidence of microphysical differences between high and low *e* days. The Ångström exponent, which is calculated, following *Bodhaine* [1996], from the total scattering coefficients measured at three wavelengths, gives a very approximate indication of particle size distribution [*Schuster et al*., 2006]. (To minimize uncertainties in the data, mean scattering is first calculated for all three wavelengths for each hour of the day and the Ångström exponent estimated from these averages). As Figure 11 shows, the Ångström exponent is much larger when *e* is high than during low *e* nights or when convective boundary layer growth is weak (i.e., during dry days at MLO). This finding indicates that a greater fraction of the aerosol population is characterized by smaller effective radii, and smaller particles are consistent with both precipitation scavenging and recent nucleation.

Of course, it is also possible that the variations in particle number concentration *cause* the differences in precipitation efficiency observed by altering the cloud droplet size distributions. Such changes might ultimately influence climate by modifying the lifetime of the clouds and thus the cloud amount [*Albrecht*, 1989]. However, differences in large-scale circulation patterns suggest a dynamical driver of Hawaiian precipitation efficiency. And, since background aerosol concentrations at MLO are similar between high and low *e* circulation patterns, it seems more likely that the observed variations in particle number concentration are the result and not the cause of the precipitation efficiency differences during this field experiment. Still, relationships among aerosols, clouds, and precipitation are not unidirectional, and aerosol changes brought about by precipitation may, in turn, influence the precipitation efficiency of the clouds in a manner that buffers the net impact on climate [*Stevens and Feingold*, 2009].

Finally, although Hawaii's unique topography no doubt enhances convective activity on the island, the fact that the convective processes evaluated in this paper are associated with robust large-scale circulation features suggests that the results presented here are representative regionally. Note, too, that increases in total column moisture during high *e* days occur over a much larger geographic area than the Hawaiian archipelago (Figure 6f). Nevertheless, a global evaluation of large-scale controls on precipitation efficiency is still needed. With satellite-borne instruments like NASA's Tropospheric Emission Spectrometer able to retrieve isotope ratios from space [e.g., *Worden et al*., 2012], future studies could expand the present analysis to a much larger geographic area and link precipitation efficiency and cloud and moisture fields on a global scale.

## 5. Conclusion

This paper has used a 3 year time series of measurements of the water vapor $^{18}O/^{16}O$ ratio to characterize the precipitation efficiency of boundary layer convection near the Mauna Loa Observatory (MLO) on the Big Island of Hawaii. Of the 74.8% of observational days during which convective boundary layer (CBL) growth was significant and defined as strong, 22.8% exhibited low precipitation efficiency (low *e*) and 18.5% high precipitation efficiency (high *e*). Days with medium values of precipitation efficiency were excluded from the analysis in order to emphasize differences between microphysical processes.

Using the isotopic information to identify synoptic drivers of precipitation efficiency, two distinct large-scale circulation patterns were identified. These suggest that low precipitation efficiency days are associated with a branching of the subtropical jet and strengthened westerly winds, which facilitate the transport of pollution from Eurasia. In contrast, high precipitation efficiency days are associated with enhanced tropical outflow, resulting in relatively clean and moist conditions. While concentrations of ozone and methane and the nighttime (background) isotope ratios reflect these distinct transport pathways, particle number concentrations appear more sensitive to local convective mixing and microphysical processes.

A single-column model demonstrated that while vertical mixing associated with strong CBL growth explains most of the diurnal variations in particle number concentration on low *e* days, it cannot replicate the diurnal patterns observed on high *e* days. During high *e* days, number concentrations declined before the peak in CBL growth and around times when precipitation was typically observed at MLO. In contrast, later in the evening, number concentrations were higher than model predictions. These discrepancies suggest that precipitation scavenging within the boundary layer may play a key role in removing preexisting aerosols and facilitating particle nucleation later in the day.

If westerly transport patterns continue to shift in frequency, for example as a result of decadal climate variability [*Lin et al*., 2014], the results of this work suggest that the prevalence of precipitation scavenging and its associated enhancement of new particles will be altered. Since number size distributions regulate aerosol direct and indirect effects, these variations could have important implications for climate. Moreover, if precipitation efficiency also influences low-cloud cover by altering vertical distributions of moisture, as recent studies claim [e.g., *Sherwood et al*., 2014; *Zhao*, 2014], these circulation changes could further modify the shortwave cloud feedback on climate. It is still unclear, however, whether reductions in precipitation efficiency will increase or decrease shortwave cloud forcing. With isotopic tracers an effective tool for characterizing precipitation efficiency and global observations of isotope ratios in water vapor available through remote sensing, future work is well poised to evaluate the relationships between precipitation efficiency and cloud properties from an observational perspective.

## Appendix A: Weighting Functions for the Single-Column Model

A single-column mixing model was developed to mimic changes in water vapor volume mixing ratio at Mauna Loa Observatory expected with the growth and collapse of the Hawaiian convective boundary layer. As shown in equation (3), the mixing coefficient (*m*, a free parameter in the model) is modified by two weighting functions—one which governs upward mixing ($w_{up}$)—or the transport of boundary layer air into the transition layer via turbulent eddies—and one which governs downward mixing ($w_{down}$)—or the diffusion of free tropospheric air into the transition layer once convection stops and downslope winds develop on the Big Island [*Garrett*, 1980].

Within the boundary layer ($z < 2000$ m, where $z$ is one of the 79 vertical levels of the column model), the weights are set to zero for all times $t$, except as follows:

$$w_{up} = 1, \quad t_{up,start} < t \leq t_{up,end}, \tag{A1}$$

where $t_{up,start}$—the time at which upward mixing starts—is a free parameter in the model and $t_{up,end}$—the time at which upward mixing ends—is set at 15:00 HST, 9 h past model initiation. Similarly, within the free troposphere ($z > z_{trans}$, where $z_{trans}$—the height at the top of the transition layer—is a free parameter in the model), the weights are set to zero for all times $t$, except as follows:

$$w_{down} = 1, \quad t_{up,end} < t < t_{down,end}\ , \tag{A2}$$

where $t_{down,end}$—the time at which downward mixing ends—is set at 24:00 HST, 18 h past model initiation.

Within the transition layer ($2000\ \text{m} \leq z \leq z_{trans}$), the weights vary linearly from zero to one as a function of time and height, following the second-order Taylor approximation of the *erf* function and mimicking the ramping

up and down of upslope and downslope flows on the Big Island. The nonzero weights are described by the following equations:

$$w_{\mathrm{up}} = \begin{cases} \left[1 - \left(\dfrac{z - z_{\mathrm{BL}}}{z_{\mathrm{trans}} - z_{\mathrm{BL}}}\right)\right]\left(\dfrac{t - t_{\mathrm{up,start}}}{t_{\mathrm{up,peak}} - t_{\mathrm{up,start}}}\right), & t_{\mathrm{up,start}} < t < t_{\mathrm{up,peak}} \\ \left[1 - \left(\dfrac{z - z_{\mathrm{BL}}}{z_{\mathrm{trans}} - z_{\mathrm{BL}}}\right)\right]\left[1 - \left(\dfrac{t - t_{\mathrm{up,peak}}}{t_{\mathrm{up,end}} - t_{\mathrm{up,peak}}}\right)\right], & t_{\mathrm{up,peak}} \le t \le t_{\mathrm{up,end}} \end{cases}, \tag{A3}$$

$$w_{\mathrm{down}} = \begin{cases} \left(\dfrac{z - z_{\mathrm{BL}}}{z_{\mathrm{trans}} - z_{\mathrm{BL}}}\right)\left(\dfrac{t - t_{\mathrm{up,end}}}{t_{\mathrm{down,peak}} - t_{\mathrm{up,end}}}\right), & t_{\mathrm{up,end}} < t < t_{\mathrm{down,peak}} \\ 1, & t_{\mathrm{down,peak}} \le t < t_{\mathrm{down,end}} \end{cases}. \tag{A4}$$

Here $t_{\mathrm{up,peak}}$—the peak of upward mixing—and $z_{\mathrm{trans}}$—the height of the top of the transition layer—are free parameters in the model; $z_{\mathrm{BL}}$ represents the top of the boundary layer (2000 m); and $t_{\mathrm{down,peak}}$—the peak of downward mixing—is set at 20:00 HST, 14 h past model initiation.

**Acknowledgments**

The authors express their sincerest thanks to P. Sheridan and J. Ogren of the NOAA-ESRL Aerosols Group: P. Sheridan prepared the 1 min Mauna Loa aerosol data set and provided essential guidance with regards to its use, while J. Ogren provided invaluable feedback on the aerosol sections of the manuscript. The authors are also most grateful to A. McClure-Begley and I. Petropavlovskikh of NOAA-ESRL for providing the Mauna Loa ozone data set and to E. Dlugokencky of NOAA-ESRL for providing the Mauna Loa methane data set. Moreover, detailed comments by two anonymous reviewers greatly improved the quality and clarity of the manuscript. Operation of the water vapor isotopic analyzer at Mauna Loa has been supported by R. Schnell and J. Barnes of NOAA-ESRL and by the NASA Tropospheric Emission Spectrometer team. Weekly calibrations of the instrument are performed by P. Sato of the NOAA Joint Institute for Marine and Atmospheric Research. The October 2010–September 2013 isotopic data may be requested by contacting the authors of this work. Funding for A. Bailey has been generously supported by a Ford Foundation Dissertation Fellowship and a NASA Earth and Space Science Fellowship.

## References

Aemisegger, F., P. Sturm, P. Graf, H. Sodemann, S. Pfahl, A. Knohl, and H. Wernli (2012), Measuring variations of $\delta^{18}$O and $\delta^{2}$H in atmospheric water vapour using two commercial laser-based spectrometers: An instrument characterisation study, *Atmos. Meas. Tech.*, *5*, 1491–1511.

Albrecht, B. (1989), Aerosols, cloud microphysics, and fractional cloudiness, *Science*, *245*, 1227–1230.

Anderson, T. L., and J. A. Ogren (1998), Determining aerosol radiative properties using the TSI 3563 integrating nephelometer, *Aerosol Sci. Technol.*, *29*, 57–69.

Bailey, A., D. Toohey, and D. Noone (2013), Characterizing moisture exchange between the Hawaiian convective boundary layer and free troposphere using stable isotopes in water, *J. Geophys. Res. Atmos.*, *118*, 8208–8221, doi:10.1002/jgrd.50639.

Bailey, A., D. Noone, M. Berkelhammer, H. C. Steen-Larsen, and P. Sato (2015), The stability and calibration of water vapor isotope ratio measurements during long-term deployments, *Atmos. Meas. Tech. Discuss.*, *8*, 5425–5466, doi:10.5194/amtd-8-5425-2015.

Bodhaine, B. A. (1996), Aerosol measurements during the Mauna Loa Photochemistry Experiment 2, *J. Geophys. Res.*, *101*, 14,757–14,765, doi:10.1029/95JD02045.

Cau, P., J. Methven, and B. Hoskins (2007), Origins of dry air in the tropics and subtropics, *J. Clim.*, *20*, 2745–2759, doi:10.1175/JCLI4176.1.

Clarke, A. D. (1993), Atmospheric nuclei in the Pacific midtroposphere: Their nature, concentration, and evolution, *J. Geophys. Res.*, *98*, 20,633–20,647, doi:10.1029/93JD00797.

Dansgaard, W. (1964), Stable isotopes in precipitation, *Tellus*, *16*, 436–468.

DeMaria, M., and J. Kaplan (1994), A Statistical Hurricane Intensity Prediction Scheme (SHIPS) for the Atlantic Basin, *Weather Forecasting*, *9*, 209–220, doi:10.1175/1520-0434(1994)009<0209:ASHIPS>2.0.CO;2.

Dlugokencky, E. J., L. P. Steele, P. M. Lang, and K. A. Masarie (1995), Atmospheric methane at Mauna Loa and Barrow Observatories: Presentation and analysis of in situ measurements, *J. Geophys. Res.*, *100*, 23,103–23,113, doi:10.1029/95JD02460.

Dlugokencky, E. J., A. M. Crotwell, P. M. Lang, and K. A. Masarie (2014), Atmospheric methane dry air mole fractions from quasi-continuous measurements at Barrow, Alaska and Mauna Loa, Hawaii, version: 2014-08-12, October 2010 to September 2013, Natl. Oceanic and Atmos. Admin., Earth Syst. Res. Lab. Global Monit. Div., Boulder, Colo.

Elison Timm, O., M. Takahashi, T. W. Giambelluca, and H. F. Diaz (2013), On the relation between large-scale circulation pattern and heavy rain events over the Hawaiian Islands: Recent trends and future changes, *J. Geophys. Res. Atmos.*, *118*, 4129–4141, doi:10.1002/jgrd.50314.

Ferrier, B. S., J. Simpson, and W.-K. Tao (1996), Factors responsible for precipitation efficiencies in midlatitude and tropical squall simulations, *Mon. Weather Rev.*, *124*, 2100–2125, doi:10.1175/1520-0493(1996)124<2100:FRFPEI>2.0.CO;2.

Galewsky, J., M. Strong, and Z. D. Sharp (2007), Measurements of water vapor D/H ratios from Mauna Kea, Hawaii, and implications for subtropical humidity dynamics, *Geophys. Res. Lett.*, *34*, L22808, doi:10.1029/2007GL031330.

Garrett, A. J. (1980), Orographic cloud over the eastern slopes of Mauna Loa volcano, Hawaii, related to insolation and wind, *Mon. Weather Rev.*, *108*, 931–941.

Gedzelman, S. D. (1988), Deuterium in water vapor above the atmospheric boundary layer, *Tellus*, *40B*, 134–147.

Harris, J. M., and J. D. Kahl (1990), A descriptive atmospheric transport climatology for the Mauna Loa Observatory, using clustered trajectories, *J. Geophys. Res.*, *95*, 13,651–13,667, doi:10.1029/JD095iD09p13651.

Harris, J. M., P. P. Tans, E. J. Dlugokencky, K. A. Masarie, P. M. Lang, S. Whittlestone, and L. P. Steele (1992), Variations in atmospheric methane at Mauna Loa Observatory related to long-range transport, *J. Geophys. Res.*, *97*, 6003–6010, doi:10.1029/92JD00158.

Hegg, D. A., L. F. Radke, and P. V. Hobbs (1990), Particle production associated with marine clouds, *J. Geophys. Res.*, *95*, 13,917–13,926, doi:10.1029/JD095iD09p13917.

Hoppel, W. A., G. M. Frick, and R. E. Larson (1986), Effect of nonprecipitating clouds on the aerosol size distribution in the marine boundary layer, *Geophys. Res. Lett.*, *13*, 125–128, doi:10.1029/GL013i002p00125.

Johnson, L. R., Z. D. Sharp, J. Galewsky, M. Strong, A. D. Van Pelt, F. Dong, and D. Noone (2011), Hydrogen isotope correction for laser instrument measurement bias at low water vapor concentration using conventional isotope analyses: Application to measurements from Mauna Loa Observatory, Hawaii, *Rapid Commun. Mass Spectrom.*, *25*, 608–616.

Jouzel, J., and L. Merlivat (1984), Deuterium and oxygen 18 in precipitation: Modeling of the isotopic effects during snow formation, *J. Geophys. Res.*, *89*, 11,749–11,757, doi:10.1029/JD089iD07p11749.

Khain, A. P. (2009), Notes on state-of-the-art investigations of aerosol effects on precipitation: A critical review, *Environ. Res. Lett.*, *4*, 015004, doi:10.1088/1748-9326/4/1/015004.

Kleissl, J., R. E. Honrath, M. P. Dziobak, D. Tanner, M. Val Martín, R. C. Owen, and D. Helmig (2007), Occurrence of upslope flows at the Pico mountaintop observatory: A case study of orographic flows on a small, volcanic island, *J. Geophys. Res.*, *112*, D10S35, doi:10.1029/2006JD007565.

Lau, K. M., and H. T. Wu (2003), Warm rain processes over tropical oceans and climate implications, *Geophys. Res. Lett.*, *30*(24), 2290, doi:10.1029/2003GL018567.

Lin, M., L. W. Horowitz, S. J. Oltmans, A. M. Fiore, and S. Fan (2014), Tropospheric ozone trends at Mauna Loa Observatory tied to decadal climate variability, *Nat. Geosci.*, *7*, 136–143, doi:10.1038/ngeo2066.

Lis, G., L. I. Wassenaar, and M. J. Hendry (2008), High-precision laser spectroscopy D/H and $^{18}O/^{16}O$ measurements of microliter natural water samples, *Anal. Chem.*, *80*, 287–293, doi:10.1021/ac701716q.

McClure-Begley, A., I. Petropavlovskikh, and S. Oltmans (2014), NOAA Global Monitoring Surface Ozone Network, October 2010 to September 2013, Natl. Oceanic and Atmos. Admin., Earth Syst. Res. Lab. Global Monit. Div., Boulder, Colo., doi:10.7289/V57P8WBF.

Mendonca, B. G., and W. T. Iwaoka (1969), The trade wind inversion at the slopes of Mauna Loa, Hawaii, *J. Appl. Meteorol.*, *8*, 213–219, doi:10.1175/1520-0450(1969)008<0213:TTWIAT>2.0.CO;2.

Merrill, J. T., M. Uematsu, and R. Bleck (1989), Meteorological analysis of long range transport of mineral aerosols over the North Pacific, *J. Geophys. Res.*, *94*, 8584–8598, doi:10.1029/JD094iD06p08584.

Nilsson, E. D., Ü. Rannik, M. Kulmala, G. Buzorius, and C. D. O'Dowd (2001), Effects of continental boundary layer evolution, convection, turbulence, and entrainment, on aerosol formation, *Tellus, Ser. B*, *53*, 441–461, doi:10.1034/j.1600-0889.2001.530409.x.

Noone, D. (2012), Pairing measurements of the water vapor isotope ratio with humidity to deduce atmospheric moistening and dehydration in the tropical midtroposphere, *J. Clim.*, *25*, 4476–4494.

Noone, D., et al. (2011), Properties of air mass mixing and humidity in the subtropics from measurements of the D/H isotope ratio of water vapor at the Mauna Loa Observatory, *J. Geophys. Res.*, *116*, D22113, doi:10.1029/2011JD015773.

Oltmans, S. J., D. J. Hofmann, J. A. Lathrop, J. M. Harris, W. D. Komhyr, and D. Kuniyuki (1996), Tropospheric ozone during Mauna Loa Observatory Photochemistry Experiment 2 compared to long-term measurements from surface and ozonesonde observations, *J. Geophys. Res.*, *101*, 14,569–14,580, doi:10.1029/95JD03004.

Oltmans, S. J., et al. (2004), Tropospheric ozone over the North Pacific from ozonesonde observations, *J. Geophys. Res.*, *109*, D15S01, doi:10.1029/2003JD003466.

Oltmans, S. J., et al. (2006), Long-term changes in tropospheric ozone, *Atmos. Environ.*, *40*, 3156–3173.

Perry, K. D., and P. V. Hobbs (1994), Further evidence for particle nucleation in clear air adjacent to marine cumulus clouds, *J. Geophys. Res.*, *99*, 22,803–22,818, doi:10.1029/94JD01926.

Perry, K. D., T. A. Cahill, R. C. Schnell, and J. M. Harris (1999), Long-range transport of anthropogenic aerosols to the National Oceanic and Atmospheric Administration baseline station at Mauna Loa Observatory, Hawaii, *J. Geophys. Res.*, *104*, 18,521–18,533, doi:10.1029/1998JD100083.

Ramanathan, V., P. J. Crutzen, J. T. Kiehl, and D. Rosenfeld (2001), Aerosols, climate, and the hydrological cycle, *Science*, *294*, 2119–2124, doi:10.1126/science.1064034.

Rambo, J., C.-T. Lai, J. Farlin, M. Schroeder, and K. Bible (2011), On-site calibration for high precision measurements of water vapor isotope ratios using off-axis cavity-enhanced absorption spectroscopy, *J. Atmos. Oceanic Technol.*, *28*, 1448–1457, doi:10.1175/JTECH-D-11-00053.1.

Ridley, B. A., E. L. Atlas, J. G. Walega, G. L. Kok, T. A. Staffelbach, J. P. Greenberg, F. E. Grahek, P. G. Hess, and D. D. Montzka (1997), Aircraft measurements made during the spring maximum of ozone over Hawaii: Peroxides, CO, $O_3$, $NO_y$, condensation nuclei, selected hydrocarbons, halocarbons, and alkyl nitrates between 0.5 and 9 km altitude, *J. Geophys. Res.*, *102*, 18,935–18,961, doi:10.1029/97JD01345.

Schuster, G. L., O. Dubovik, and B. N. Holben (2006), Angstrom exponent and bimodal aerosol size distributions, *J. Geophys. Res.*, *111*, D07207, doi:10.1029/2005JD006328.

Sherwood, S. C., R. Roca, T. M. Weckwerth, and N. G. Andronova (2010), Tropospheric water vapor, convection, and climate, *Rev. Geophys.*, *48*, RG2001, doi:10.1029/2009RG000301.

Sherwood, S. C., S. Bony, and J.-L. Dufresne (2014), Spread in model climate sensitivity traced to atmospheric convective mixing, *Nature*, *505*, 37–42, doi:10.1038/nature12829.

Steen-Larsen, H. C., et al. (2013), Continuous monitoring of summer surface water vapor isotopic composition above the Greenland Ice Sheet, *Atmos. Chem. Phys.*, *13*, 4815–4828, doi:10.5194/acp-13-4815-2013.

Stevens, B., and G. Feingold (2009), Untangling aerosol effects on clouds and precipitation in a buffered system, *Nature*, *461*, 607–613, doi:10.1038/nature08281.

Sturm, P., and A. Knohl (2010), Water vapor $\delta^2H$ and $\delta^{18}O$ measurements using off-axis integrated cavity output spectroscopy, *Atmos. Meas. Tech.*, *3*, 67–77.

Sui, C.-H., X. Li, M.-J. Yang, and H.-L. Huang (2005), Estimation of oceanic precipitation efficiency in cloud models, *J. Atmos. Sci.*, *62*, 4358–4370, doi:10.1175/JAS3587.1.

Sui, C.-H., X. Li, and M.-J. Yang (2007), On the definition of precipitation efficiency, *J. Atmos. Sci.*, *64*, 4506–4513, doi:10.1175/2007JAS2332.1.

Thornton, D. C., A. R. Bandy, B. W. Blomquist, J. D. Bradshaw, and D. R. Blake (1997), Vertical transport of sulfur dioxide and dimethyl sulfide in deep convection and its role in new particle formation, *J. Geophys. Res.*, *102*, 28,501–28,509, doi:10.1029/97JD01647.

Tremoy, G., F. Vimeux, O. Cattani, S. Mayaki, I. Souley, and G. Favreau (2011), Measurements of water vapor isotope ratios with wavelength-scanned cavity ring-down spectroscopy technology: New insights and important caveats for deuterium excess measurements in tropical areas in comparison with isotope-ratio mass spectrometry, *Rapid Commun. Mass Spectrom.*, *25*, 3469–3480.

Twomey, S. (1977), The influence of pollution on the shortwave albedo of clouds, *J. Atmos. Sci.*, *34*, 1149–1152.

Wen, X.-F., X. Lee, X.-M. Sun, J.-L. Wang, Y.-K. Tang, S.-G. Li, and G.-R. Yu (2012), Intercomparison of four commercial analyzers for water vapor isotope measurement, *J. Atmos. Oceanic Technol.*, *29*, 235–247.

Wood, R., D. Leon, M. Lebsock, J. Snider, and A. D. Clarke (2012), Precipitation driving of droplet concentration variability in marine low clouds, *J. Geophys. Res.*, *117*, D19210, doi:10.1029/2012JD018305.

Worden, J., S. Kulawik, C. Frankenberg, V. Payne, K. Bowman, K. Cady-Peirara, K. Wecht, J.-E. Lee, and D. Noone (2012), Profiles of $CH_4$, HDO, $H_2O$, and $N_2O$ with improved lower tropospheric vertical resolution from Aura TES radiances, *Atmos. Meas. Tech.*, *5*, 397–411, doi:10.5194/amt-5-397-2012.

Yu, H., et al. (2006), A review of measurement-based assessments of the aerosol direct radiative effect and forcing, *Atmos. Chem. Phys.*, *6*, 613–666, doi:10.5194/acp-6-613-2006.

Zhao, M. (2014), An investigation of the connections among convection, clouds, and climate sensitivity in a global climate model, *J. Clim.*, *27*, 1845–1862, doi:10.1175/JCLI-D-13-00145.1.